PAPER

Check for updates

Electrocatalytic oxidation or amidation of olefins by asymmetric electrolytes steering carbocation pathways

Yingxuan Zhao,† Chenyang Shen,† Qing Liu, Siyuan Zhao, Ruiyao Zhao, Xiangke Guo, Nianhua Xue, Luming Peng, [ID] Xuefeng Guo, [ID] Yan Zhu [ID] and Weiping Ding [ID] *

Olefin functionalization is a powerful approach for accessing a wide range of value-added compounds with broad applications. Advanced electrosynthesis offers streamlined upgrades over traditional methods by employing electrons as traceless agents and is extremely attractive for promoting olefin functionalization, but achieving high efficiency and selectivity remains a major challenge. Here, we report a conceptually new electrochemical strategy that precisely controls the reactivity of olefin-derived carbocations, the key intermediates of functional transformations, through asymmetric electrolyte design. Using cyclohexene as a model substrate, we reveal that while the local electrode microenvironment steers surface-generated carbocations toward either electrochemical oxidation or Ritter-type amidation in water/acetonitrile mixed electrolytes, the intrinsic competition between water and acetonitrile fundamentally dictates the reaction outcome. By creating a controlled molecular imbalance under overall charge neutrality through selective semipermeable membranes, the asymmetric electrolyte system decouples these competing pathways, enabling exclusive oxidation or 98% selective amidation—the highest Ritter-type amidation efficiency reported under electrochemical conditions. This work establishes electro-driven carbocation control as a powerful principle for resolving intrinsic selectivity challenges in multicomponent systems and provides a broadly applicable, sustainable strategy for selective olefin electro-conversion.

Green foundation

1. This work advances green chemistry by introducing an asymmetric electrolyte-regulated electrochemical approach to precisely control carbocation reactivity, enabling highly selective olefin functionalization using electrons as traceless reagents and avoiding use of stoichiometric oxidants or organic solvent and harsh conditions.

2. Using asymmetric electrolyte made of water and solvent easy to handle, the system achieves up to 100% selectivity for electrochemical olefin oxidation or 98% selectivity for Ritter-type amidation with water or acetonitrile as benign O/N sources, representing the highest efficiency reported for electrochemical Ritter amidation under mild conditions.

3. Greenness of production of high value chemicals could be further enhanced by coupling the process with renewable electricity, expanding the use of sustainable olefin feedstocks and implementing continuous-flow electrochemical techniques for more energy efficiency and greater scale.

1. Introduction

The electrification of chemical synthesis through green electrocatalysis is transforming modern chemical manufacturing, offering sustainable, resource-efficient, and energy-conscious pathways.[1–6] Olefins stand out as indispensable molecular scaffolds in both petrochemical production and pharmaceutical

innovation.[7–10] Their direct functionalization provides efficient access to α,β-unsaturated carbonyls and allylic amines—structural motifs widely present in bioactive molecules and functional materials.[11–15] However, the high bond dissociation energies and weak polarity of C–H bonds impose steep thermodynamic and kinetic barriers.[16,17] Moreover, the coexistence of multiple reactive pathways complicates selectivity, making olefin electrofunctionalization a longstanding challenge.

Recent advances in this field have emerged from three main strategies: (i) surface catalysis on metals and their derivatives, (ii) mediator-assisted pathways, and (iii) direct substrate electrooxidation. Noble metals such as Pd and Pt, along with

Key Lab of Mesoscopic Chemistry, School of Chemistry and Chemical Engineering, Nanjing University, Nanjing 210023, China. E-mail: dingwp@nju.edu.cn
† These authors contributed equally to this work.

their derivatives,[18–20] enable selective reactions *via* adsorption and surface reactions. Alternatively, redox mediators such as NHPI[21,22] TEMPO,[23,24] and various metal salts or their complexes[25–28] can participate in redox cycling or interact with substrates to produce highly reactive intermediates that drive the reaction forward. In contrast, direct electrooxidation affords carbocationic or radical intermediates that undergo nucleophilic capture in solution, thereby streamlining functionalization.[29] Notably, carbocations can be generated electrochemically under mild conditions without strongly acidic media, greatly expanding synthetic scope.[30] Yet, their high reactivity often triggers uncontrolled pathways, such as indiscriminate nucleophilic attack, rearrangements, and eliminations, making downstream selectivity largely dictated by the intrinsic properties of these intermediates.[31–33] These difficulties are amplified in the presence of multiple nucleophiles, especially when weak nucleophiles initiate the reaction, as exemplified in Ritter-type reaction.[34–36]

Unlike conventional homogeneous liquid-phase chemistry, electrochemical systems offer unique opportunities to reshape reaction landscapes through electrolyte and cell engineering. For instance, H-type cells equipped with ion-exchange membranes maintain global charge balance while creating local compositional asymmetry, effectively decoupling reaction events. Analogous strategies are already established in energy storage, such as acid–base electrolyte configurations that enable Zn/Mn batteries to reach voltages far exceeding those achievable with conventional electrolytes.[37] Translated into synthetic contexts, this electrochemical asymmetry provides a powerful lever for carbocation control: it enables spatial and kinetic separation between carbocation generation and nucleophilic interception, thereby optimizing capture efficiency, modulating reaction rates, and steering product selectivity. In this way, electrochemical platforms not only overcome long-standing challenges in carbocation chemistry but also establish new design principles for selective olefin functionalization.

Herein, we employ cyclohexene (CHX) as a model substrate to investigate electrochemical carbocation chemistry. Carbon paper electrodes are identified as efficient materials for promoting carbocation generation and subsequent functionalization. Water acts as the oxygen source for the electrochemical cyclohexene oxidation reaction (ECOR), while acetonitrile functions both as co-solvent and nucleophile, enabling the electrochemical Ritter-type cyclohexene amidation reaction (ECAR) *via* carbocation capture. Mechanistic insights derived from *in situ* diffuse reflectance infrared Fourier transform spectroscopy (DRIFTS) and computational modeling reveal that the kinetics of ECOR and ECAR are strongly influenced by the local microenvironment at the electrode–electrolyte interface. Guided by these findings, we design an asymmetric H-type electrolyte reactor in which a cation-exchange membrane separates two chambers containing water/acetonitrile mixtures with distinct compositions. The defining feature of this configuration is not simple physical separation, but the deliberate creation of local solvent and nucleophilicity asymmetry under overall charge neutrality. This design allows precise modu-

lation of local nucleophilicity, steering carbocation interception toward the desired pathway and boosting ECAR selectivity from 64% to 98%, while achieving switchable ECOR selectivity of 100% and overall faradaic efficiencies (F.E.) of up to 65%. The overall process is depicted in Scheme 1.

2. Experimental section

2.1 Reagents and materials

Cyclohexene (CHX, inhibitor-free, 99%) was purchased from Sigma-Aldrich. Anhydrous acetonitrile (CH_3CN, 99.8%, $H_2O \leq$ 0.001%), 2-cyclohexen-1-ol (**1**, 95%), 2-cyclohexen-1-one (**2**, 97%), cyclopentanecarbaldehyde (**3**, 98%), cyclohexanone (**4**, 99.8%), heavy-oxygen water ($H_2^{18}O$, 97%), ferric oxide (α-Fe_2O_3, 30 nm, 99.5%), cobalt oxide (Co_3O_4, 99.9%), titanium oxide (TiO_2, 60 nm, anatase, 99.8%), vanadium oxide (V_2O_5, 99.99%), tungsten oxide (WO_3, 99.8%), sodium perchlorate ($NaClO_4$, 99%), sodium trifluoromethanesulfonate ($NaCF_3SO_3$, 98%), sodium tetrafluoroborate ($NaBF_4$, 99%), sodium hexafluorophosphate ($NaPF_6$, 98%), tetrabutylammonium perchlorate (Bu_4NClO_4, 99%), tetrabutylammonium trifluoromethanesulfonate ($Bu_4NCF_3SO_3$, 98%), tetrabutylammonium tetrafluoroborate (Bu_4NBF_4, 98%), tetrabutylammonium hexafluorophosphate (Bu_4NPF_6, 99%), perchloric acid ($HClO_4$, 70%) and Nafion 117 solution (~5% in a mixture of lower aliphatic alcohols and water) were purchased from Aladdin. *N*-Acetyl-2-cyclohexen-1-amine (**5**) was synthesized using a method reported in the literature.[38] The ^1H NMR and ^{13}C NMR spectra are shown in Fig. S8. Alcohol (EtOH, 99%) and Nitrobenzene ($PhNO_2$, 99%) were purchased from Sinopharm Chemical Reagent Co. Ltd. The metal–nitrogen–carbon materials (Fe-NC, Cu-NC) were synthesized using the method previously developed by our group.[39,40] $LaFeO_3$ and CuBTC were synthesized using the method previously reported.[41,42] Carbon paper (CP, TPG-H-060) was purchased from Toray Industries, Inc. Ti mesh was purchased from Kunshan Fuershun Electronic Materials Co., Ltd. Glassy carbon plate (GCP) and glassy carbon electrode (GCE, 3 mm diameter) was purchased from GaossUnion Technology Co., Ltd. Milli-Q water (18.2 MΩ cm) was used for electrolytes containing water. All reagents were of analytical grade and used without further purification.
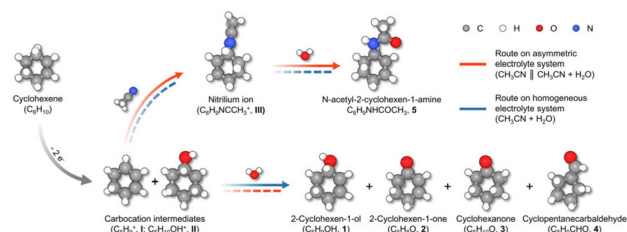
Scheme 1 Schematic show of reaction process. Pathways of CHX oxidation or amidation in asymmetric and symmetric electrolytes. Solid lines: favored; dashed lines: suppressed.

2.2 Catalytic electrode preparation

A series of potential active materials were firstly screened, including oxides (often used as catalysts for olefin oxidation), metal–nitrogen–carbon materials and common precious metal catalysts.[43–46] For the powder catalyst (TiO_2, Fe_2O_3, Co_3O_4, $LaFeO_3$, WO_3, V_2O_5, CuBTC, Fe-NC, and Cu-NC), the catalytic electrodes were prepared by drop casting method. Briefly, 2 mg catalyst was dispersed in 1.0 ml 0.05 wt% Nafion/EtOH solution by sonication for 1 hour. The prepared catalyst ink was drop-cast onto a 1×2 cm piece of carbon paper, covering an area of 1 cm^2 with a loading of 1 mg cm^{-2}. Precious metal (Ru, Pd) catalytic electrodes were prepared on carbon paper by electrodeposition with a loading of ~1 mg cm^{-2}. Oxidized carbon paper (O-CP) was obtained by treating the carbon paper with Fenton's reagent for 3 hours.

2.3 Electrochemical measurements

Data were acquired on a CHI760e electrochemical measurements (CH Instruments). All electrochemical tests were conducted using a three-electrode system with a double salt bridge Ag/AgCl (8060-2, provided by GaossUnion) reference electrode (the external salt bridge solution is saturated potassium nitrate to prevent the influence of Cl$^-$ ions on the electrochemical system). CP was used as the counter electrode.

For the single-cell electrochemical cyclohexene oxidation reaction (ECOR), an undivided electrochemical cell was used, with an electrolyte consisting of a 9/1 volume ratio of CH_3CN/H_2O, containing 0.1 M $NaClO_4$ or $HClO_4$. Prior to assessing the ECOR activity of various materials, the electrodes were activated via cyclic voltammetry (0–1.8 V vs. Ag/AgCl, scan rate of 50 mV s^{-1}, 20 cycles). The catalytic activity of the materials was evaluated using linear sweep voltammetry (LSV) in the potential range of 0–1.8 V (vs. Ag/AgCl) at a scan rate of 10 mV s^{-1}, both before and after the addition of 0.1 M CHX. The product was enriched by constant potential electrolysis at 1.7 V (vs. Ag/AgCl) with a charge of 200C.

The kinetic measurements of ECOR were conducted on a glassy carbon electrode with a CP loading of 0.1 mg cm^{-2} to obtain more accurate values. The apparent activation energy (E_a) of ECOR can be obtained from the current density at different temperatures using the Arrhenius equation:

$$E_a = 2.3R[\partial(\log j)/\partial(-1/T)]_{E,C}$$

According to Marcus theory,[47] for an outer-sphere electron transfer reaction, the activation energy E_a is related to the applied potential as follows:

$$E_a = [\lambda - F(E - E^\circ)]^2/4\lambda$$

where λ is the solvent reorganization energy and E° is the thermodynamic equilibrium potential. Consequently, for an outer-sphere electron transfer, $E_a^{1/2}$ exhibits a linear relationship with the applied potential E.

For the single-cell electrochemical cyclohexene amidation reaction (ECAR), the difference from ECOR is that product 5 is formed when the water content is below 2.5 vol%. However, when

the water content reaches 0.5 vol% or lower, the selectivity for product 5 no longer increases, stabilizing at approximately 60%.

For the asymmetric H-cell ECAR, a Nafion 117 membrane was used as the cation exchange membrane. The anode solution consisted of 0.1 M $NaClO_4$ dissolved in anhydrous acetonitrile, while the cathode solution was a 0.1 M $NaClO_4$ acetonitrile solution containing 40 μL of H_2O. During electrolysis, 200 μL of CHX was added to the anode compartment. The product was enriched by applying a constant potential of 1.7 V (vs. Ag/AgCl) with a charge of 200C.

2.4 General characterization

X-ray photoelectron spectroscopy (XPS) was performed on a Thermo Scientific K-Alpha instrument using an excitation source of Al Kα-rays (hv = 1486.6 eV). All the spectra were calibrated with the C 1s peak (284.8 eV) binding energy as the energy standard.

Scanning Electron Microscope (SEM) were conducted using Hitachi S-4800 at 5 kV.

UV–Vis spectra were recorded on a Shimadzu UV-1800 with a low sampling scan rate.

The ^{1}H- and ^{13}C-NMR spectra were measured on a Bruker Avance 400 spectrometer. Auto phase correction and baseline correction were conducted using MestReNova software prior to the integration of each peak in the spectra.

Gas chromatography (GC) analyses were performed using a GC 9860 chromatograph, equipped with a flame ionization detector and an SE-54 capillary column (30 m × 0.25 mm × 0.25 μm) for the separation and quantitative analysis of products. Nitrobenzene was used as the internal standard to quantify the substrate and products. The faradaic efficiency (F. E.) of the reaction is calculated using the following formula:

$$\text{F.E.}_{\text{products}} (\%) = \text{mol of products}/[\text{passed charge}/(n \times F)] \times 100\%,$$

where n represents the number of electrons transferred to produce the respective product. For product 2, $n = 4$, whereas for products 1, 3, 4, and 5, $n = 2$.

Gas Chromatography-Mass Spectrometry Measurements (GC-MS) were measured on Shimadzu Nexis GC-2030 with a flame ionization detector and SH-Rtx-1 capillary column (30 m × 0.25 mm × 0.25 μm). The MS conditions were as follows: ion source temperature was set to 200 °C, and the mass acquisition range was from 45 to 250 m/z.

CHX temperature-programmed desorption (TPD) was carried out using a gas chromatograph equipped with a thermal conductivity detector. CP was pretreated under Ar at 350 °C for 30 min to remove surface adsorbates and then cooled to room temperature. CHX was introduced via a bubbler for 30 min to achieve adsorption, followed by an Ar purge to remove physisorbed species. TPD measurements were conducted from room temperature to 500 °C at a heating rate of 10 °C min^{-1} under a continuous Ar flow of 30 mL·min^{-1}.

Fourier transform infrared (FTIR) spectroscopy was performed on a NEXUS 870 spectrometer equipped with an atte-

nuated total reflectance (ATR) accessory, with a scanning range of 500–4000 cm^{-1}.

In situ diffuse reflectance infrared Fourier transform spectroscopy (DRIFTS) measurements were carried out using a Thermo Scientific Nicolet iS50 FTIR spectrometer equipped with an MCT detector cooled by liquid N_2 and an *in situ* reaction cell (Hefei *In situ* Technology). Prior to measurements, CP were pretreated at 200 °C for 1 h under a N_2 flow to remove surface adsorbates. During the tests, both the working and counter electrodes were CP, with Ag/AgCl serving as the reference electrode:

1. Detection of carbocations. With 10% water content, 0.1 M CHX was introduced, and the background spectrum was recorded in the absence of applied potential. *In situ* infrared spectra were then collected under open-circuit potential (OCP) and at applied potentials of 1.0, 1.2, 1.4, 1.6, and 1.8 V (*vs.* Ag/AgCl).

2. Detection of intermediates during electrolysis. With 0.5% water content, 0.1 M CHX was introduced, and the background spectrum was recorded without applied potential. *In situ* infrared spectra were subsequently collected at a fixed potential of 1.7 V (*vs.* Ag/AgCl) at both the anode and cathode.

All *in situ* infrared spectra were acquired by recording 32 scans at a resolution of 2 cm^{-1}.

2.5 Computational details

All the DFT calculations were carried out using the Vienna *ab initio* simulation package (VASP 5.4.4).[48,49] The generalized gradient approximation (GGA) with Perdew–Burke–Ernzerhof (PBE) functional[50] was adopted to describe the exchange correlation energy, while the ion-core electronic interactions were treated by the projected augmented wave (PAW) method.[51] A plane wave basis with a kinetic energy cutoff of 400 eV and the Brillouin zone was sampled with a Γ-centered (3 × 3 × 1) *k*-point mesh for geometry optimization. The convergence criteria for atomic relaxation were 1×10^{-5} eV of energy and 0.03 eV Å^{-1} of force, respectively. All transition states were located based on the climbing image nudged elastic band (CI-NEB)[52] combined with the improved dimer method (IDM),[53] and then confirmed by only one imaginary frequency for each state.

3. Results and discussion

3.1. Catalyst screening and reaction mechanism

A series of materials were screened for the ECOR, with the linear sweep voltammetry (LSV) results shown in Fig. S1a–c. ECOR activity was evaluated from the difference in current density before and after the addition of CHX at fixed oxidation potentials (1.8 V *vs.* Ag/AgCl under neutral conditions and 2.15 V *vs.* Ag/AgCl under acidic conditions, Fig. S1d). Among the tested materials, carbon paper (CP) delivered the highest J_{ECOR}. Under neutral conditions, the carbon electrode exhibited an anodic current increase starting at ~1.5 V (*vs.* Ag/AgCl), due to the oxygen evolution reaction (OER). Upon introducing 0.1 M CHX, the onset potential shifted negatively to ~1.3 V (*vs.* Ag/AgCl), accompanied by a marked increase in current density. In contrast, when Pt sheet, Fe_2O_3 or other electrode

materials were used, the polarization curves showed negligible differences with or without CHX, indicating that ECOR occurs exclusively on CP.

The electrochemical oxidation products of CHX under neutral conditions at a charge of 200C (~50% conversion) were analyzed and quantified by gas chromatography-mass spectrometry (GC-MS) and the results are depicted in Fig. 1a. The predominant products were identified as 2-cyclohexen-1-ol (**1**), 2-cyclohexen-1-one (**2**), cyclohexanone (**3**), and cyclopentanecarbaldehyde (**4**). The overall faradaic efficiency (F.E.) reached 60–75% at 1.5 V–1.7 V (Fig. 1b), while it slightly decreased to ~50% at a higher potential of 1.8 V due to the aggravation of side reaction OER. At a given oxidation potential (*e.g.*, 1.8 V) and prolonged time of reaction (Fig. 1c), an increase in the relative abundance of product **2** accompanied by a decrease in product **1**, indicating that **2** is formed *via* further oxidation of its alcohol precursor. In contrast, products **3** and **4** remained essentially constant once generated, suggesting that they are formed directly from CHX rather than *via* secondary transformations. Notably, product **4** possesses a five-membered ring, implying that its formation involves a ring contraction rearrangement. We propose this occurs through an unstable carbocation intermediate undergoing a nucleophilic rearrangement analogous to a pinacol-type rearrangement, consistent with the mechanism reported by Shono and other researchers.[54,55]

Since OER is an unavoidable competing process during ECOR, we examined whether hydroxyl radicals (˙OH) contribute to the reaction. The variation of ECOR faradaic efficiency during electrolysis is shown in Fig. 1d. The carbon electrode maintained an F.E. exceeding 30% throughout, reaching over 70% in the initial stage, a trend inconsistent with a typical ˙OH-driven pathway. Moreover, no hydrogen peroxide species was detected during the entire ECOR process (Fig. S2), further excluding a radical-based mechanism. Oxygen isotope labeling was then performed: when $H_2^{18}O$ was replaced with $H_2^{16}O$, the *m/z* values of product fragments shifted by +2 units (Fig. S3), demonstrating that the oxygen atoms in the products originate from water in the electrolyte. To assess the influence of electrode structure on ECOR, four different carbon materials, including CP, oxygen-rich carbon paper (O-CP), graphite rod (GR), and glassy carbon plates (GCP) were evaluated. All these materials exhibited clear ECOR activity (Fig. S4). Although the current response varied in magnitude, the product distributions were nearly identical, indicating that selectivity is relatively insensitive to electrode surface structure and that ECOR does not follow Langmuir–Hinshelwood mechanism. Moreover, temperature-programmed desorption (TPD) of CHX on CP showed a desorption peak at ~60 °C (Fig. S5), suggesting CHX weak physisorption rather than strong chemisorption on CP surface.

Additional electrochemical kinetic parameters of ECOR were measured. From LSV curves in 0.1 M NaClO$_4$, acetonitrile/water of 9/1 (v./v., all ratios mentioned hereafter are volume ratios.) mixed electrolyte (Fig. S6a), a near first-order dependence on CHX was obtained from the log(J_{ECOR}) *versus*
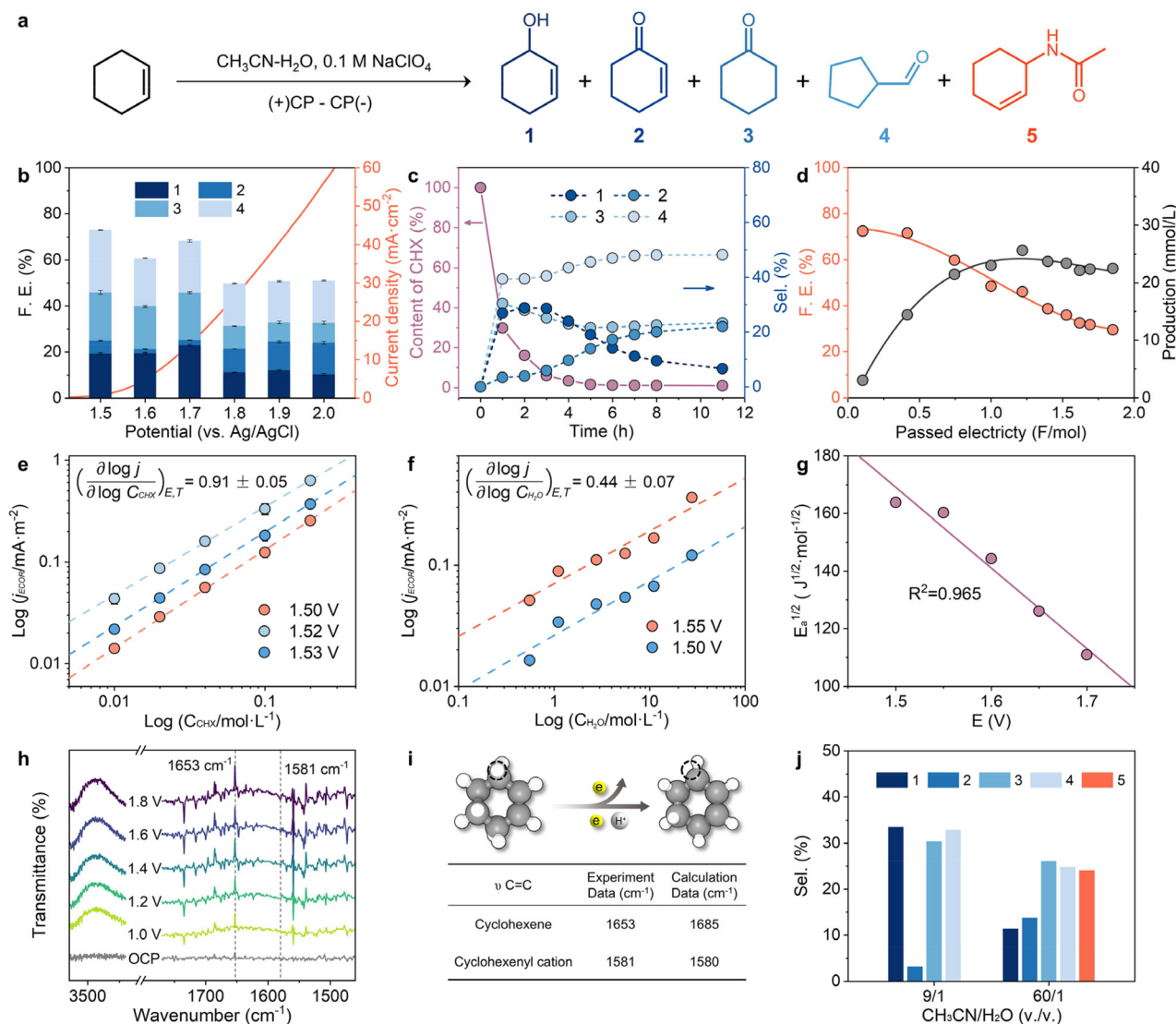
Fig. 1 Electrocatalytic performance of CHX functionalization. (a) Products of the electrochemical oxidation of CHX on CP in 0.1 M NaClO$_4$, CH$_3$CN/H$_2$O = 9/1 (v/v) electrolyte; (b) the relationship between the total yield of products and F.E. at 1.8 V (*vs.* Ag/AgCl) concerning the electricity passed; (c) F.E. of various products at different potentials during the charge of 200C; (d) the time-dependent relationship between the yield of individual products at 1.8 V (*vs.* Ag/AgCl) and the conversion rate of CHX. Kinetic data of CHX electrochemical oxidation in 0.1 M NaClO$_4$, CH$_3$CN/H$_2$O = 9/1 (v/v) electrolyte on glass carbon electrode. (e) Corresponding CHX concentration dependence of oxidation current; (f) corresponding H$_2$O concentration dependence of oxidation current; (g) linear fitting of $E_a^{1/2}$ as a function of applied potential (*E*); (h) *in situ* DRIFTS spectra recorded at different potentials (*vs.* Ag/AgCl) when CP is used as the anode; (i) structures of CHX and the cyclohexenyl cation, and the corresponding theoretically simulated infrared absorption signals; (j) products of ECOR on CP under the electrolyte compositions of CH$_3$CN/H$_2$O = 9/1 (v/v) and CH$_3$CN/H$_2$O = 60/1 (v/v).

log (C_{CHX}) plot (Fig. 1e), while the reaction order with respect to water was determined to be 0.44.(Fig. 1f and S6b). The Tafel slope of ECOR on CP was 120 mV per decade (Fig. S6c), suggesting that the rate-determining step (RDS) contains an electron transfer with no prior electron transfer before RDS.[56] The peak current density (J_p) exhibited a linear dependence on the square root of scan rate ($\nu^{1/2}$), consistent with diffusion-controlled processes at peak potentials (Fig. S6d–f). By varying the system temperature, the apparent activation energy (E_a) of ECOR at different potentials was evaluated (Fig. S7). According to Marcus theory,[47] the E_a of an outer-sphere electron transfer

process exhibits a quadratic dependence on the applied potential (*E*). When $E_a^{1/2}$ was plotted against *E* (Fig. 1g), a well-defined linear correlation (R^2 = 0.965) was observed, indicating that the electron transfer in ECOR on CP proceeds *via* an outer-sphere mechanism.

Collectively, these results demonstrate that CHX is only weakly adsorbed on CP, where it undergoes outer-sphere electron transfer to generate reactive intermediates that subsequently react with water to form oxidation products. The presence of such intermediates was verified by *in situ* DRIFTS. As shown in Fig. 1h, increases in transmittance correspond to

the consumption of vibrational modes, while decreases correspond to the emergence of new species. Aside from the signals corresponding to known products (vC=O around 1730 cm^{-1}; δC–H around 1400 cm^{-1}), a new infrared absorption signals emerged at 1580 cm^{-1} after the potential exceeded 1.4 V, corresponding to the calculated vC=C of the carbocationic intermediate (Fig. 1i). Although carbocations are typically short-lived, the allylic carbocation is stabilized by conjugation between the positive center and the C=C bond, enabling detection. The emergence of this signal coincided with attenuation of the CHX vC=C and water vO–H bands, confirming that the reaction proceeds *via* the proposed carbocationic pathway, dominated by liquid-phase reactions between the cyclohexenyl carbocation and water.

As a highly reactive intermediate, the carbocation can also undergo nucleophilic attack by other species. In current mixed electrolyte, acetonitrile is less nucleophilic than water and typically does not participate. However, by increasing the proportion of acetonitrile to water in the electrolyte (CH$_3$CN/H$_2$O = 9/1 to CH$_3$CN/H$_2$O = 60/1, Fig. 1j), an ECAR has been discovered, wherein acetonitrile and water reacts with cyclohexenyl cation to yield *N*-acetyl-2-cyclohexen-1-amine (**5**, CHXAM) in high selectivity, which can serve as a distinctive building block in the realms of organic synthesis and pharmaceutical development. It is a Ritter-type reaction,[57] but without presence of any strong inorganic acid which is necessary for Ritter reaction.

Based on these results, the reaction network and mechanism of ECOR and ECAR on CP are proposed and shown in Fig. 2. Key intermediates are carbocations I and II generated by electron transfer from CHX, with the initial electron transfer being the RDS. At higher water content (CH$_3$CN/H$_2$O = 9/1), intermediate II is attacked by water to yield product **1**, which can be further oxidized to product **2**. Intermediate I may undergo deprotonation to form product **3** or rearrangement followed by water attack to generate product **4**. Under low-water conditions (CH$_3$CN/H$_2$O = 60/1), the carbocation intermediate is instead attacked by acetonitrile to afford a nitrilium ion(III), which subsequently reacts with water to give the amide product **5**. Because CHX interacts only weakly with CP, the electron transfer proceeds *via* an outer-sphere mechanism.
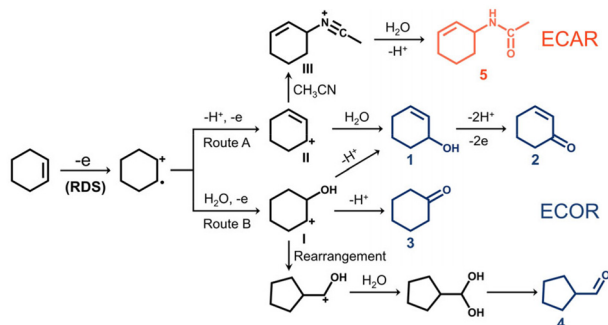
This mechanistic framework rationalizes the observed product distributions and their dependence on potential and time, while highlighting the distinctive activity of carbon-based electrodes: weak intermolecular interactions (*e.g.*, π–π stacking) activate CHX, while surface paramagnetic centers efficiently mediate electron transfer and stabilize carbocationic intermediates.[58] In contrast, metal electrodes (*e.g.*, Pt) or metal oxide electrodes (*e.g.*, TiO$_2$), where CHX adsorbs too strongly or exhibits electronic mismatch, fail to stabilize carbocations, and therefore lack significant ECAR or ECOR activity.

3.2 Electrode microenvironment effects on ECOR and ECAR kinetics

The acetonitrile content in the solution affects the selectivity to product **5** (Fig. 3a and Table S1). When the CH$_3$CN/H$_2$O ratio reaches 200/1, the selectivity to product **5** approaches ~60%. Further reduction in the water content, down to the stoichiometry required for the reaction (0.2 vol%), however, does not lead to higher amide selectivity. According to the pro-
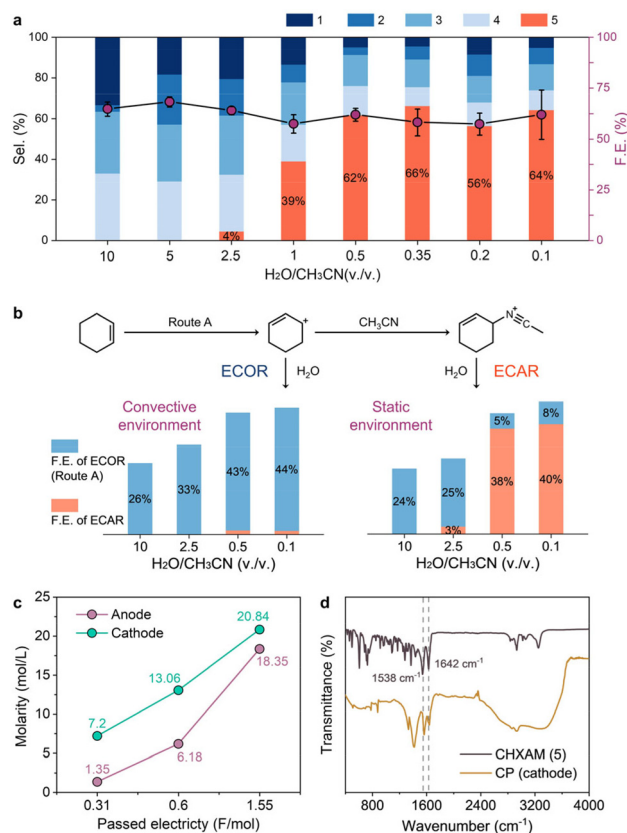

Fig. 3 Seletivities of products of electrocatalytic reactions of CHX and process characterization. (a) With varied ratio of water/acetonitrile; (b) static and convection at stirring of 600 rpm in a single electrochemical cell; (c) with an H-cell equipped with a Nafion 117 membrane, the variation of concentration of amide products in the anodic and cathodic regions. (d) FTIR spectra of the cathodic electrode after electrolysis. All electrolysis was performed on CP at a potential of 1.7 V (*vs.* Ag/AgCl) with a charge of 200C, using 0.1 M NaClO$_4$ as the supporting electrolyte.

Fig. 2 Reaction network chart. The reaction trigger, key intermediates and pathways for ECOR and ECAR.

posed reaction network, we know that ECOR and ECAR are initiated by cyclohexyl carbocations(ɪ and ɪɪ) and nitrilium ions (ɪɪɪ), respectively. The reaction kinetics of these species should significantly affect the selectivity of ECOR and ECAR. It was found that, in the single electrolytic cell, the strong convection induced by stirring leads to suppression of the ECAR process, as shown in Fig. 3b and Table S2. When only ECOR occurs ($H_2O/CH_3CN \geq 2.5$ vol%), the process is largely unaffected by convection. However, in cases where ECAR becomes significant ($H_2O/CH_3CN < 2.5$ vol%), convection almost completely suppresses the formation of product **5**, while dramatically increasing the selectivity for product **1**. Given that product **1** originates from ECOR *via* pathway A, this observation suggests that ECOR (route A) and ECAR may exhibit different sensitivities to the local reaction environment (local pH or local concentration of substances).

To evaluate the influence of local pH, Table S3, entry 1, 2 and 3 shows that under convective conditions, keeping the local substance concentrations as constant, the introduction of 0.1 M $HClO_4$ effectively activates ECAR, at which acidity, notably, carbocations cannot be formed by acid catalysis from CHX and are still electrochemically generated, as illustrated in Fig. S8. Considering the ECOR (route A) and ECAR share common cyclohexyl carbocation intermediates(ɪɪ), it is reasonable to suggest that the acid facilitates the formation of nitrilium ion intermediates(ɪɪɪ) from cyclohexyl carbocations(ɪɪ). This facilitation is likely due to the competitive reaction, where the deprotonation step of water's nucleophilic attack on the cyclohexyl carbocation(ɪɪ) is hindered by the high proton concentration under acidic conditions.

The H-cell equipped with a cation exchange membrane simulated the local distribution of substrate in a static single electrolytic cell, enabling the separate analysis of the ECAR process at both the anode and cathode. As shown in Table S3, entry 4, under stirring conditions, the H-cell with a Nafion 117 membrane detects both oxidation and amide products (Sel. > 50%) at both electrode regions, indicating that, in addition to protons, intermediates from both the ECOR and ECAR processes can permeate through the cation exchange membrane. Though protons diffuse rapidly due to the stirring, reducing the acid-promoting effect on ECAR, a significant amount of amide product **5** is still observed in the anode region, likely due to the consumption of water in the anode, leading to a rapid decrease in local water content. This depletion forces the carbocations(ɪɪ) in the anode region to react with acetonitrile, resulting in the formation of nitrilium ion(ɪɪɪ).

Besides, Fig. 3c illustrates that the concentration of product **5** in the cathode region exceed those in the anode region. Under conditions of Table S3, entries 4, significant deposits were observed on the cathode after prolonged electrolysis, while the anode remained clean (SEM images and photos shown in Fig. S9a and b). Fourier transform infrared (FTIR) spectroscopy analysis (Fig. 3d) and X-ray photoelectron spectroscopy (XPS) (Fig. S9c) revealed that the deposits on the cathode exhibited amide characteristic bands consistent with those of product **5** at ~1538 cm^{-1} and ~1642 cm^{-1} and the red

shifts were caused by their polymerization *via* intermolecular hydrogen bonding of amide groups. This hydrogen-bond-induced polymerization phenomenon confirms that the product **5** exists at high concentration at the cathode, consistent with results abovementioned. Such findings suggest that the cathodic environment may offer additional facilitation for the ECAR process. A supposed explanation, based on the ECAR reaction pathway, is that the cathodic region generates residual OH^- (whereas both protons and carbocations are produced at the anode, only hydroxide ions are generated at the cathode). These excess OH^- preferentially attack the nitrilium ion(ɪɪɪ), resulting in a higher rate of amide formation compared to the anode, leading to differential product concentrations at the anode and cathode.

In situ DRIFTS provides an accurate reflection of the corresponding signals for the amide product **5** at both the anode and cathode, as illustrated in Fig. 4a and b. The time-dependent infrared signals at a fixed potential (Fig. 4c–f) demonstrate that at the cathode, the characteristic bands of the amide (νC=O at 1653 cm^{-1} and δN–H at 1539 cm^{-1}) emerge slightly earlier than those at the anode. Furthermore, the signal for acetonitrile (νC≡N) at the cathode displays a diminishing trend, signifying the consumption of nitrilium ion(ɪɪɪ) at this electrode. This observation strongly suggests that the pivotal nucleophilic attack by water on the nitrilium ion(ɪɪɪ) in ECAR predominantly occurs at the cathodic interface. In contrast, the signal for νC≡N at the anode shows an increasing trend, attributable to the consumption of water and the consequent rise in acetonitrile concentration near the electrode. The data strongly support the hypothesis that the basicity of the cathodic region accelerates the final nucleophilic step of ECAR, consistent with the experimental phenomena described above.

Density functional theory (DFT) calculations were performed to evaluate each elementary step in the ECOR (route A) and ECAR reactions, aiming to assess the intrinsic solution-phase reactivity trends of the corresponding intermediates. As shown in Fig. 4g, the activation barrier the reaction between the carbocation(ɪɪ) and water is 0.46 eV (TS1–IS1), which is lower than that for acetonitrile (0.84 eV, TS2–IS1). This result indicates that carbocations(ɪɪ) preferentially undergo the ECOR process under mixed solvent conditions, which is align with previous experimental observations. This also provides explanation to why even at high acetonitrile concentrations, the nucleophilic attack of water on the carbocation(ɪɪ) is still faster than that of acetonitrile. Regarding the reactions of water with the nitrilium ion(ɪɪɪ) and the carbocation(ɪɪ), it is found the barrier for the reaction between water and the nitrilium ion(ɪɪɪ) is only 0.11 eV (TS3–FS2), lower than the aforementioned 0.46 eV for the carbocation(ɪɪ). Therefore, when the intermediates formed in the anode diffuse to the cathode under the influence of the electric field, nitrilium ions(ɪɪɪ) are more readily attacked by water, leading to the observed cathodic promotion on the ECAR process.

Noteworthy that no amines or hydroxylamines were detected in the cathodic region (Fig. S10), ruling out the possi-
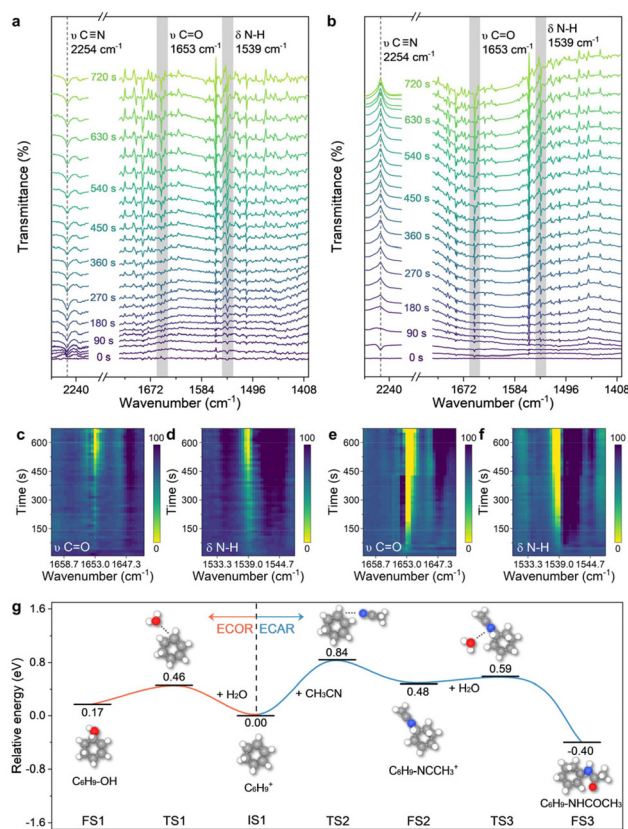
Fig. 4 *In situ* DRIFTS analysis of intermediates during electrolysis and theoretical calculations. At 1.7 V *vs.* Ag/AgCl in 0.1 M NaClO$_4$ with an H$_2$O/CH$_3$CN = 1/200 electrolyte. (a and b) Time-resolved *in situ* DRIFTS spectra recorded at the anode and cathode, respectively, with baseline subtraction performed against the spectrum collected after the addition of CHX but prior to potential application (a decrease/increase in transmittance corresponds to an increase/decrease in the intensity of the corresponding signals); (c–f) time-dependent evolution of amide characteristic peaks at the anode and cathode, with the color scale representing relative transmittance; (g) density functional theory (DFT) calculations of energy barriers for key steps of reaction involving carbocations(II) in ECOR and ECAR.

bility of amide formation through the coupling of cathodic and anodic products. Therefore, the unique electrode microenvironment plays a critical role in the ECAR kinetics, as illustrated in Fig. 5. In a local steady-state electrochemical cell, without direct strong convection between the anode and cathode, two key steps of the ECAR process are established: (1) the local proton-rich, water-poor environment at the anode suppresses the formation of intermediate I and inhibits water's nucleophilic attack on carbocations(I,II), while promoting acetonitrile attack to generate nitrilium ions(III); (2) nitrilium ions(III) diffuse to the cathode under the influence of local electric field and react with OH$^-$ generated at the cathode to form amides right away. The coupling of local environments at the anode and cathode accelerates the ECAR process.

Previous studies have shown that the nature of the supporting electrolyte can modulate the hydrophilicity of the electro-
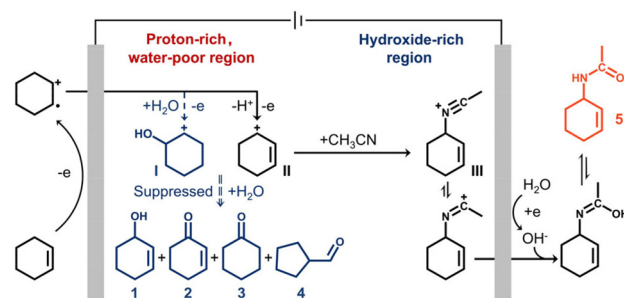

Fig. 5 Diagram illustration on the coorperation between the two electrode regions. In a local steady-state electrochemical cell, the proton-rich, water-poor anode region suppresses intermediate I and water nucleophilic attack in ECOR, favoring nitrilium ion(III) formation. The hydroxide-rich cathode region promotes product 5 formation, and the interplay between anode and cathode environments accelerates the ECAR process. Solid lines indicate facilitating pathways, while dashed lines represent inhibitory pathways.

chemical double layer, thereby influencing the kinetics and selectivity of electrochemical reactions.[59] Therefore, we sought to reduce the water content in the anodic double layer by employing hydrophobic electrolytes, with the aim of enhancing the efficiency of acetonitrile capture, relevant data are presented in Fig. S11. Changing the anion hydrophobicity had little effect on ECAR selectivity. However, replacing Na$^+$ with the hydrophobic tetra-*n*-butylammonium (Bu$_4$N$^+$) led to a significant decrease in ECAR selectivity (*e.g.*, product 5 decreased by 18% with Bu$_4$NClO$_4$ and 28% with Bu$_4$NOTf), which appears contrary to our initial expectation. Nevertheless, this outcome aligns with our proposed mechanism, where CHX oxidation proceeds *via* two pathways: A and B, with the latter requiring water. On carbon electrodes, olefins do not directly bind to the surface, electron transfer proceeds *via* an outer-sphere mechanism. The resulting radical cation intermediates, cationic intermediates I and II are generated in the outer Helmholtz plane (OHP). During anodic oxidation (anions accumulate in the inner Helmholtz plane (IHP), whereas cations are excluded to the OHP), the presence of hydrophobic cations such as Bu$_4$N$^+$ significantly reduces the water content near the OHP, thereby suppressing oxidation pathway B. Grouping products 1, 2, and 5, which share a common intermediate, reveals that hydrophobic cations promote the formation of intermediate II *via* pathway A (*e.g.*, selectivity increased by 20% and 14% with Bu$_4$NClO$_4$ and Bu$_4$NOTf, respectively). Once intermediate II is formed, it diffuses from the OHP into the bulk solution, where it is captured by either water or acetonitrile. Due to the weaker solvation of hydrophobic cations, nucleophilic sites of water molecules become more exposed, favoring nucleophilic attack by water. As a result, switching the cation to Bu$_4$N$^+$ promotes oxidation pathway A but reduces the selectivity for ECAR product 5. These findings support the proposed mechanism and suggest that under single-cell conditions, further enhancement of ECAR efficiency may be inherently limited.

3.3 Asymmetric electrolyte system for highly selective functionalization and expanding reaction scope

Based on the disclosed mechanism, the kinetics of ECOR and ECAR exhibit distinct sensitivities to the electrode microenvironment. In a homogeneous cell, it is difficult to achieve fine control over these processes. However, an electrochemical system need not remain homogeneous, in an H-type cell equipped with a semipermeable membrane, local imbalances of reactive species can be established while maintaining overall ionic charge balance. To exploit this feature, an asymmetric H-type electrochemical cell was deliberately constructed, with a cation exchange membrane controlling the electrolyte compositions in the anode and cathode chambers to maximize the ECAR process, as shown in Fig. 6a. The anodic chamber was filled with anhydrous acetonitrile, whereas the cathodic chamber contained acetonitrile mixed with the stoichiometric amount of water required for amide formation. The inset photograph clearly illustrates the local imbalance of species within this asymmetric electrolyte cell during electrolysis: the anodic solution appears red, while the cathodic solution remains colorless.

The anhydrous anodic environment decouples the competing ECOR and ECAR pathways and ensures that only carbocations(II) and nitrilium ions(III) are generated, which subsequently diffuse toward the cathode under the electric field and readily react with OH^- to form amides. Compared with the conventional homogeneous electrolyte system (Fig. 6b), the asymmetric electrolyte system dramatically enhanced ECAR performance: the selectivity for amide product **5** increased from 64% to 98%, while the F.E. rose from 64% to 71%, representing the highest selectivity reported to date in electrochemical systems (Table S4). When the solvent in the anode chamber was adjusted to acetonitrile containing >2.5 vol% water, the electrolysis switched to a complete ECOR process affording 100% oxidation products with F.E. $\geq$ 65%.

To assess solvent sustainability, long-term electrolysis was performed (Fig. S12). As the substrate was gradually consumed, a noticeable decrease in reaction current was observed. However, upon replenishment of CHX and water through electrolyte replacement, the current returned to its initial value. This recovery was reproducible over multiple cycles, highlighting the robustness and regenerative potential of the system under prolonged operation.

Under similar conditions, we investigated the selective functionalization of four additional representative olefins on CP (Table S5). Cyclic olefins, such as methylcyclopentene and cyclooctene, exhibited clear electrooxidation and amidation reactivity, whereas linear olefins, exemplified by 1-hexene, showed no detectable electrochemical response. DFT calculations (Fig. S13) reveal that electron transfer from linear olefins to the carbon electrode involves a substantially higher energy barrier, accounting for their inactivity. In addition, olefins lacking α-hydrogens, such as styrene, fail to undergo electrochemical amidation due to the inability to generate the requisite carbocation intermediates. These results delineate the substrate scope of CP-catalyzed olefin functionalization and further substantiate the proposed carbocation-mediated mechanism.

Fig. 6 System-level working principle and performance comparison of the reaction setup. (a) The asymmetric electrolyte cell enables a highly selective ECAR process, the inset photograph shows the anodic chamber solution appears light red, while the cathodic chamber remains colorless. (b) An ordinary homogeneous electrolyte system enables a limited selective ECAR process. In the asymmetric electrolyte system, the solvent in the anode chamber is anhydrous acetonitrile, while the solvent in the cathode chamber is a mixture of acetonitrile with the stoichiometric amount of water required for the reaction. In the ordinary symmetric electrolyte system, the solvents in both the anode and cathode chambers are mixtures of acetonitrile with 0.1 vol% water. The supporting electrolyte is 0.1 M NaClO₄, and the F.E. and selectivity of amide product were measured under test conditions of 1.7 V (vs. Ag/AgCl) with a total charge of 200C.

4. Conclusions

The electrochemical platform presented in this work enables precise control of carbocation pathways through an asymmetric electrolyte system, achieving selective olefin functionalization. Using CHX as a model substrate, carbon electrodes were identified as optimal electrocatalysts, promoting the formation of carbocation intermediates. Mechanistic insights, supported by reaction process analysis, *in situ* spectroscopy, and computational modeling, reveal that ECOR is a purely anodic process, wherein carbocations undergo nucleophilic attack by water. In contrast, ECAR involves a coupled process, integrating contributions from both anodic and cathodic microenvironments. The asymmetric electrolyte system, with distinct compositions in the H-cell anode and cathode chambers, allows precise control over carbocation transformation. The anodic chamber facilitates the generation of nitrilium ions, whereas the cathodic chamber enhances the nucleophilic attack of acetonitrile on nitrilium ions, achieving up to 98% selectivity for ECAR. The broad applicability to cyclic olefins highlights the generality of this methodology, offering a versatile platform for synthesizing allylic oxygenates or
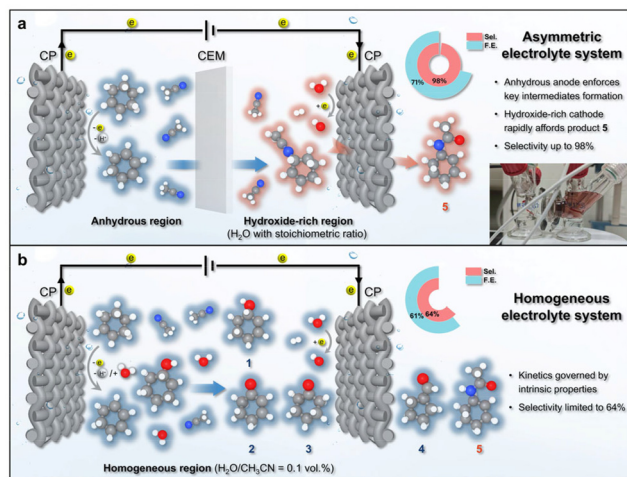
amides. Crucially, the dual-function electrolyte design (H_2O as green oxygen source/CH_3CN as solvent-reagent hybrid) embodies atom-economic principles, while membrane-enabled reaction compartmentalization eliminates cross-nucleophile interference. This new paradigm of asymmetric electrolyte systems provides a blueprint for sustainable olefin functionalization beyond traditional redox mediators.

Author contributions

Y. X. Z. and C. Y. S. contributed equally to this work. The manuscript was written through contributions of all authors. All authors have given approval to the final version of the manuscript.

Conflicts of interest

The authors declare no conflict of interest.

Data availability

The data supporting this article have been included as part of the supplementary information (SI). Supplementary information is available. The Supplementary Information includes detailed product analysis, featuring GC signals of products 1–5 and the ^1H NMR, ^{13}C NMR, and MS spectra of product 5. It also provides supplementary figures and tables covering catalyst screening, materials characterization (SEM and XPS), reaction-related analyses (hydrogen peroxide detection, isotopic distribution, material comparisons, TPD analysis, kinetic and activation energy studies, electrolyte effects, long-term stability tests, DFT calculations, and product distribution under varied conditions.), literature comparisons, and substrate scope verification. See DOI: https://doi.org/10.1039/d5gc07050c.

Acknowledgements

References

1 P. De Luna, C. Hahn, D. Higgins, S. A. Jaffer, T. F. Jaramillo and E. H. Sargent, *Science*, 2019, **364**, eaav3506.

2 D. J. Davidson, *Nat. Energy*, 2019, **4**, 254–256.

3 T. H. Meyer, I. Choi, C. Tian and L. Ackermann, *Chem*, 2020, **6**, 2484–2496.

4 S. D. Minteer and P. Baran, *Acc. Chem. Res.*, 2020, **53**, 545–546.

5 D. S. Cardoso, B. Sljukic, D. M. Santos and C. A. Sequeira, *Org. Process Res. Dev.*, 2017, **21**, 1213–1226.

6 Y. Mei, P. Liao and Y. Zhang, *Org. Biomol. Chem.*, 2025, **23**, 9752–9780.

7 S. A. Chernyak, M. Corda, J. P. Dath, V. V. Ordomsky and A. Y. Khodakov, *Chem. Soc. Rev.*, 2022, **51**, 7994–8044.

8 C. S. Higman, J. A. Lummiss and D. E. Fogg, *Angew. Chem., Int. Ed.*, 2016, **55**, 3552–3565.

9 T. F. Degnan Jr, *Curr. Opin. Chem. Eng.*, 2015, **9**, 75–82.

10 D. L. Golden, S. E. Suh and S. S. Stahl, *Nat. Rev. Chem.*, 2022, **6**, 405–427.

11 S. Zhang, H. Neumann and M. Beller, *Chem. Soc. Rev.*, 2020, **49**, 3187–3210.

12 D. J. Wang, K. Targos and Z. K. Wickens, *J. Am. Chem. Soc.*, 2021, **143**, 21503–21510.

13 R. H. Grubbs, *Angew. Chem., Int. Ed.*, 2006, **45**, 3760–3765.

14 I. M. Taily, D. Saha and P. Banerjee, *Org. Lett.*, 2022, **24**, 2310–2314.

15 Y. Wang, S. Dana, H. Long, Y. Xu, Y. Li, N. Kaplaneris and L. Ackermann, *Chem. Rev.*, 2023, **123**, 11269–11335.

16 K. J. Jiao, Y. K. Xing, Q. L. Yang, H. Qiu and T. S. Mei, *Acc. Chem. Res.*, 2020, **53**, 300–310.

17 F. Wang and S. S. Stahl, *Acc. Chem. Res.*, 2020, **53**, 561–574.

18 M. Chung, J. H. Maalouf, J. S. Adams, C. Jiang, Y. Román-Leshkov and K. Manthiram, *Science*, 2024, **383**, 49–55.

19 Y. Lum, J. E. Huang, Z. Wang, M. Luo, D. H. Nam, W. R. Leow, B. Chen, J. Wicks, Y. C. Li and Y. Wang, *Nat. Catal.*, 2020, **3**, 14–22.

20 A. Winiwarter, L. Silvioli, S. B. Scott, K. Enemark-Rasmussen, M. Sarić, D. B. Trimarco, P. C. Vesborg, P. G. Moses, I. E. Stephens and B. Seger, *Energy Environ. Sci.*, 2019, **12**, 1055–1067.

21 E. J. Horn, B. R. Rosen, Y. Chen, J. Tang, K. Chen, M. D. Eastgate and P. S. Baran, *Nature*, 2016, **533**, 77–81.

22 T. Shen, J. Zhao, X. Ren, Z.-Q. Liu and S. Liu, *J. Org. Chem.*, 2025, **90**, 1148–1158.

23 C. Li, C. C. Zeng, L. M. Hu, F. L. Yang, S. J. Yoo and R. D. Little, *Electrochim. Acta*, 2013, **114**, 560–566.

24 K. S. Lee, F. Barbieri, E. Casali, E. T. Marris, G. Zanoni and J. M. Schomaker, *J. Am. Chem. Soc.*, 2024, **147**, 318–330.

25 A. Das, J. E. Nutting and S. S. Stahl, *Chem. Sci.*, 2019, **10**, 7542–7548.

26 T. Shen and T. H. Lambert, *J. Am. Chem. Soc.*, 2021, **143**, 8597–8602.

27 T. Shen and T. H. Lambert, *Science*, 2021, **371**, 620–626.

28 K. Mitsudo, T. Kaide, E. Nakamoto, K. Yoshida and H. Tanaka, *J. Am. Chem. Soc.*, 2007, **129**, 2246–2247.

29 Y. Imada, Y. Okada, K. Noguchi and K. Chiba, *Angew. Chem., Int. Ed.*, 2019, **58**, 125–129.

30 B. C. Hawkins, J. M. Chalker, M. L. Coote and A. C. Bissember, *Angew. Chem.*, 2024, **136**, e202407207.

31 R. R. Naredla and D. A. Klumpp, *Chem. Rev.*, 2013, **113**, 6905–6948.

32 S. Y. Hong, D. Kim and S. Chang, *Nat. Catal.*, 2020, **4**, 79–88.

33 W. Huang, D. He, H. Jiang and W. Wu, *Chem. Soc. Rev.*, 2025, **54**, 10724–10795.

34 Y. Xu, Q. Li, R. Ye, B. Xu and X. Zhou, *J. Org. Chem.*, 2023, **88**, 9518–9522.

35 L. Zhang, Y. Fu, Y. Shen, C. Liu, M. Sun, R. Cheng, W. Zhu, X. Qian, Y. Ma and J. Ye, *Nat. Commun.*, 2022, **13**, 4138.

36 L. Zhu, F. Guo, W. Luo, S. Xie, T. Zhu, Z. Liao, B. Xiong, Y. Liu, K.-W. Tang and R. Qiu, *Green Chem.*, 2025, **27**, 11125–11132.

37 C. Zhong, B. Liu, J. Ding, X. Liu, Y. Zhong, Y. Li, C. Sun, X. Han, Y. Deng and N. Zhao, *Nat. Energy*, 2020, **5**, 440–449.

38 X. Xiong, J. Wong and Y.-Y. Yeung, *J. Org. Chem.*, 2021, **86**, 6974–6982.

39 Q. Liu, Y. Xu, Y. Zhao, K. Wang, C. Liang, S. Zhao, X. Wang, X. Guo, N. Xue and W. Ding, *Adv. Mater. Technol.*, 2023, **8**, 2202007.

40 Y. Xu, Y. Yan, M. Pang, L. Wang, Y. Zhao, C. Deng, Y. Cui, X. Guo, P. Wang and W. Ding, *Appl. Surf. Sci.*, 2021, **560**, 150054.

41 M. Wu, S. Chen and W. Xiang, *Chem. Eng. J.*, 2020, **387**, 124101.

42 A. Vishnyakov, P. I. Ravikovitch, A. V. Neimark, M. Bülow and Q. M. Wang, *Nano Lett.*, 2003, **3**, 713–718.

43 Y. Zhao, C. Deng, D. Tang, L. Ding, Y. Zhang, H. Sheng, H. Ji, W. Song, W. Ma and C. Chen, *Nat. Catal.*, 2021, **4**, 684–691.

44 R. Nie, J. Shi, W. Du, W. Ning, Z. Hou and F.-S. Xiao, *J. Mater. Chem. A*, 2013, **1**, 9037–9045.

45 M. Jafarpour, A. Rezaeifard, M. Ghahramaninezhad and F. Feizpour, *Green Chem.*, 2015, **17**, 442–452.

46 K. Alexopoulos, M. F. Reyniers and G. B. Marin, *J. Catal.*, 2012, **289**, 127–139.

47 R. A. Marcus, *J. Chem. Phys.*, 1956, **24**, 966–978.

48 G. Kresse and J. Furthmüller, *Phys. Rev. B: Condens. Matter Mater. Phys.*, 1996, **54**, 11169.

49 G. Kresse and J. Furthmüller, *Comput. Mater. Sci.*, 1996, **6**, 15–50.

50 J. P. Perdew, K. Burke and M. Ernzerhof, *Phys. Rev. Lett.*, 1996, **77**, 3865.

51 P. E. Blöchl, *Phys. Rev. B: Condens. Matter Mater. Phys.*, 1994, **50**, 17953.

52 G. Henkelman and H. Jónsson, *J. Chem. Phys.*, 2000, **113**, 9978–9985.

53 G. Henkelman and H. Jónsson, *J. Chem. Phys.*, 1999, **111**, 7010–7022.

54 T. Shono and A. Ikeda, *J. Am. Chem. Soc.*, 1972, **94**, 7892–7898.

55 C. M. Elliott, J. Dunkle and S. Paulson, *Langmuir*, 2005, **21**, 8605–8608.

56 A. J. Bard and L. R. Faulkner, in *Electrochemical Methods, Fundamentals and Applications*, John Wiley & Sons, Inc.: Phoenix, 2nd edn, 2001.

57 J. J. Ritter and P. P. Minieri, *J. Am. Chem. Soc.*, 1948, **70**, 4045–4048.

58 I. F. Hu and T. Kuwana, *Anal. Chem.*, 1986, **58**, 3235–3239.

59 F. Dorchies, A. Serva, D. Crevel, J. De Freitas, N. Kostopoulos, M. Robert, O. Sel, M. Salanne and A. Grimaud, *J. Am. Chem. Soc.*, 2022, **144**, 22734–22746.